THESIS FOR THE DEGREE OF LICENTIATE OF PHILOSOPHY

Theoretical and computational advances in small-angle x-ray scattering tensor tomography

Leonard C. Nielsen

Department of Physics
Chalmers University of Technology
Gothenburg, Sweden, 2022

Theoretical and computational advances in small-angle x-ray scattering tensor tomography

Leonard C. Nielsen

Department of Physics

Chalmers University of Technology
SE-412 96 Gothenburg, Sweden
Phone: +46 (0)31 772 1000
www.chalmers.se

Chalmers, Chalmers Digitaltryck
Gothenburg, Sweden, May 2022

Abstract

The relationships between microscopic and macroscopic structures is a central topic of materials physics. Small-angle x-ray scattering (SAXS) is a powerful experimental technique for probing and mapping variations in electron density, given by the reciprocal space map, down to the nanometer scale in two dimensions. SAXS tensor tomography combines this mapping with tomographic techniques to yield a three-dimenisonal reconstruction of the reciprocal space map. The development of an improved method for SAXS tensor tomographic reconstruction using a basis of real spherical harmonics has yielded faster and more accurate reconstructions with a more detailed representations of the reciprocal space map. The reconstructed reciprocal space maps yielded by RUSHTT can be further analyzed to quantify their degree of symmetry, and retrieve complex features such as multiple orientations within a single volume element. Moreover, the development of a mathematical framework for SAXS tensor tomography using spherical harmonics in terms of integral geometry has furthered understanding of the method's possibilities and constraints.

Keywords: tensor tomography, reciprocal space map, small-angle scattering

List of Publications

This thesis is based on the following publications:

[A] **Leonard C. Nielsen**, Paul Erhart, Manuel Guizar-Sicairos, Marianne Liebi, "Improved small-angle x-ray scattering tensor tomography with unrestricted spherical harmonics". Manuscript.

[B] **Leonard C. Nielsen**, Paul Erhart, Esther Tsai, Mirko Holler, Manuel Guizar-Sicairos, Marianne Liebi , "Sub-voxel analysis of orientations in Small-Angle X-ray Scattering Tensor Tomography". Manuscript.

Acknowledgments

I would like to thank my supervisor Marianne Liebi for her considerate, open and empathetic approach to her role as supervisor and group leader, and for trusting me in steering the direction of this project.

Moreover, I am grateful to my co-supervisor Paul Erhart for his thoughtful and enthusiastic supervision of my coding, valuable input on every layer of abstraction, and tireless correction of my LaTeX syntax.

Finally, I want to thank my wife, Hezhe, for always supporting me, especially throughout this stressful period.

Contents

CHAPTER 1

Background

The relationship between microscopic and macroscopic material properties is one of the principal overarching topics of materials physics. Understanding how the structural components of complex materials are arranged at multiple scales is key both to understanding materials in nature, such as animal tissues, and to developing and characterizing novel synthetic materials. Small-angle X-ray Scattering (SAXS) is a powerful method for probing the reciprocal space map (RSM) of a sample, which yields information about the arrangement of structural elements down to the nanometer scale [1]–[3]. When used to scan samples, SAXS can map the change in the RSM in two dimensions across macroscopic samples, which may be several millimeters large [4]–[6]. While SAXS only probes a two-dimensional cut of the three-dimensional RSM, scanning SAXS can be combined with *tomographic* techniques to yield a three-dimensional reconstruction of the sample geometry, and the reciprocal space map of each volume element [2], [7]–[13]. This provides an excellent way to examine how the nanostructure of a sample changes throughout its volume.

Tomography, or imaging by sections, is the use of a penetrating wave (such as x-rays) to probe the interior of a sample, yielding data which may be used

to reconstruct virtual sections[1]. Traditional methods of tomography which reconstruct a scalar, such as x-ray absorption tomography, may be performed by rotating either the sample or the x-ray source about a single axis. Each slice that lies orthogonal to the axis of rotation can then be independently reconstructed, and combined to yield a full volume render of the sample. This uniaxial approach can also be used for SAXS tomography when the reciprocal space map is isotropic.

However, materials are in general *anisotropic* — they may contain oriented structural elements (such as fibres) or regular crystalline arrangements which result in electron density variations which are not uniform over all directions. There are special cases of anisotropy that can be treated using scalar tomography, such as when all parts of the sample have the same type of anisotropy and share an axis of symmetry. But in general, this problem must be approached by reconstructing a tensor in each volume element, thus leading to SAXS tensor tomography (SAXSTT). SAXSTT requires more information than scalar tomography; generally, it is not sufficient to probe the sample while rotating only about a single axis. Rather, it is necessary to include a second degree of freedom, such as a tilt axis orthogonal to the first [14]–[16].

The aim of this project is to further develop existing methods for SAXSTT, evaluate their performance, and improve theoretical understanding of the requirements of and constraints on these approaches. The purpose of this is to extend the range and amount of information that can be obtained from SAXSTT reconstructions, to gain a better understanding of the optimal experimental parameters for obtaining SAXSTT datasets, and to extend the general method to other experimental methods, such as wide-angle x-ray scattering (WAXS).

[1] The term "tomogram" is sometimes used to refer specifically to a virtual slice obtained through tomographic reconstruction, as is suggested by its etymology. However, this usage is not consistent, and some authors use it to refer to what is otherwise called a "volume render", or to any other visual representation of some subset of a tomographic reconstruction. The term is therefore avoided in this work.

CHAPTER 2

Small-angle x-ray scattering tensor tomography

2.1 SAXS at one length scale

Small-angle x-ray scattering is a powerful experimental technique for probing the nanostructure of macroscopic samples [1]–[3]. The two-dimensional scattered intensity distribution obtained from a single measurement is described by the relationship

$$I(\mathbf{q}) \propto \left| \iiint dV \left[\widetilde{\rho}(\mathbf{r})^2 e^{-i\mathbf{q}\cdot\mathbf{r}} \right] \right|,$$

where $\widetilde{\rho}(\mathbf{r})^2$ is the auto-correlation function of the electron density of the measured sample, and $\mathbf{q}$ is the reciprocal-space vector [17]. In the small-angle approximation, this corresponds to a cut of the reciprocal space map which is orthogonal to the direction of the impinging x-ray beam. The scattered part of the beam is attenuated at approximately the same rate as the transmitted part, so the contribution of each volume element to the total scattered signal is independent of depth (Figure 2.1). The scattering per volume element is

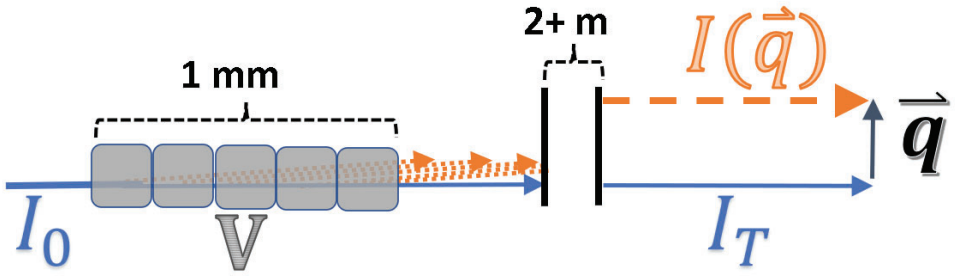

Figure 2.1: Schematic illustration of small angle scattering of a volume. A beam of intensity I_0 impinges on a volume V. Each volume element contributes to the scattered intensity $I(\mathbf{q})$ independently of its position, as the scattered intensity is attenuated at the same rate as the transmitted intensity. After traversing over a long distance (>2 m in the figure) relative to the total length of the volume (1 mm in the figure), the scattered intensity impinges on the detector approximately parallel to the transmitted intensity I_T. The displacement vector between the point of impact of the scattered and transmitted components defines the scattering vector $\mathbf{q}$ (labelled $\vec{q}$ in the figure for clarity).

therefore obtained by

$$I_N(\mathbf{q}) = \frac{I(\mathbf{q})}{I_T},$$

where I_T is the transmitted intensity of that particular measurement. In this work, we are primarily concerned with analysis of the reciprocal space map at a single $|\mathbf{q}|$. This reduces the reciprocal space map to a function on the unit sphere, spanned by the polar and azimuthal angles (θ, ϕ). Moreover, it reduces the transmission-normalized intensity $I_N(\theta, \phi)$ to a function on the unit circle. For these reasons, it becomes natural to express the reciprocal space map in a basis of real spherical harmonics as

$$M(\theta, \phi) = \sum_{\ell=0,2}^{\infty} \sum_{m=-\ell}^{\ell} a_m^\ell \, \hat{Y}_m^\ell(\theta, \phi),$$

where a_m^ℓ is a scalar coefficient and $\hat{Y}_m^\ell(\theta, \phi)$ is a real spherical harmonic basis function of order ℓ and degree m. Because the reciprocal space map is point-symmetric, the summation reduces to even ℓ. Since our ultimate goal is to describe a three-dimensional distribution of reciprocal space maps, it

is convenient to define the three-dimensional tensor field of reciprocal space maps

$$M(\mathbf{r},\theta,\phi) = \sum_{\ell=0,2}^{\infty} \sum_{m=-\ell}^{\ell} a_m^\ell(\mathbf{r})\, \hat{Y}_m^\ell(\theta,\phi),$$

where each $a_m^\ell(\mathbf{r})$ is a scalar field in three-dimensional space. In practice, measured SAXS detector images need to be reduced (by binning or fitting) into angular segments. At a single $|\mathbf{q}|$, this usually means reducing a measured distribution on the unit circle into discrete points, or, e.g., Fourier coefficients. This will limit the maximum ℓ needed to completely describe the measurement to

$$\ell_{\max} = n - 2 + p(n), \tag{2.1}$$

where n is the number of reduced data points or coefficients, and $p(n)$ is the parity function, which is 1 for n odd, and 0 for n even. We therefore obtain the model for our three-dimensional tensor field representing the distribution of reciprocal space maps for a single $|\mathbf{q}|$ of a measured sample,

$$M(\mathbf{r},\theta,\phi) = \sum_{\ell=0,2}^{\ell_{\max}} \sum_{m=-\ell}^{\ell} a_m^\ell(\mathbf{r})\, \hat{Y}_m^\ell(\theta,\phi). \tag{2.2}$$

2.2 Real spherical harmonics

The real spherical harmonics are an orthogonal basis set for functions on the unit sphere that may be regarded as the spherical equivalent of Fourier coefficients for real functions. The basis function of order ℓ and degree m has the definition

$$\hat{Y}_m^\ell(\theta,\phi) = \begin{cases} P_m^\ell(\cos\theta)\cos(m\phi), & m \geq 0. \\ P_{|m|}^\ell(\cos\theta)\sin(|m|\phi), & m < 0, \end{cases} \tag{2.3}$$

where P_m^ℓ is the associated Legendre polynomial of order ℓ and degree m. A spherical function composed from basis functions of a particular ℓ is subject to the spherical harmonic rotation theorem, which states that such a function

is invariant under the rotation of the coordinate system, in the sense that the same function can be represented using a set of basis functions with the same ℓ. The spherical harmonics have a set of associated inner products, the power spectrum functions, from which descriptive statistics of the spherical function they represent may be obtained [18]. They are defined as

$$S_\ell(Y,U) = \sum_{m=-\ell}^{\ell} \mathcal{N}(\ell) \int d\Omega \left[U_m^\ell Y_m^\ell\right], \tag{2.4}$$

where $\mathcal{N}(\ell)$ is a normalization factor that depends on the normalization chosen for the associated Legendre polynomials and $d\Omega$ is the element of solid angle. In particular,

$$\sum_{\ell=1}^{\ell_{\max}} S_\ell(Y,Y) = \mathrm{var}(Y), \tag{2.5}$$

$$\sum_{\ell=1}^{\ell_{\max}} S_\ell(Y,U) = \mathrm{cov}(Y,U), \tag{2.6}$$

where $\mathrm{var}(Y)$ and $\mathrm{cov}(Y,U)$ are the variance and covariance of Y and (Y,U), respectively. Moreover, the power spectrum functions are invariant with respect to each ℓ, such that the contribution to the variance and covariance of each order can be computed separately. In addition, the coefficient of $\hat{Y}_0^0$ precisely equals the mean of the function. Thus, we also obtain that

$$\sqrt{\sum_{\ell=0}^{\ell_{\max}} S_\ell(Y,Y)} = \mathrm{RMS}(Y) = |Y|, \tag{2.7}$$

where $\mathrm{RMS}(Y)$ is the root-mean-square of Y. Equation (2.7) thus gives the canonical inner-product norm of a reciprocal space map represented by spherical harmonics. Equations (2.5), (2.6), and (2.7) are highly useful for the comparison and evaluation of spherical harmonics, as they are invariant of the chosen coordinate system. In particular, the two equations (2.5) and (2.6) can be used to calculate the Pearson correlation coefficient between two reciprocal space maps. Moreover, the square root of the variance divided by the mean, i.e. the normalized standard deviation, can be used to quantify the

relative amount of anisotropy of a reciprocal space map.

This work involves the study of oriented samples, specifically samples with fiber symmetric reciprocal space maps. Fiber symmetry means that the volume elements of the sample exhibits transversal scattering, i.e., it scatters orthogonally to a particular direction. This orthogonal direction can be taken to define the orientation of the sample, and indeed coincides with the orientation of fiber-like nanostructural elements. The easiest way to define this orientation is in terms of the eigenvectors of the traceless rank-2 component of the tensor field, which corresponds precisely to the $\ell = 2$ spherical harmonics. The eigenvector which possesses the minimal eigenvalue defines the fiber-symmetric orientation (Paper I). A more general description of fiber orientation which includes $\ell > 2$ components may be obtained by using the Funk transform, which takes a spherical function and returns a transformed function on which the value on each point equals the integral of the great circle to which it is orthogonal on the original function. The Funk transform can be understood as transforming transversal scattering into longitudinal scattering (see Paper II).

2.3 Tensor tomography

Tomography, or imaging by probing the interior of a sample through the use of a penetrating wave, encompasses a wide range of different methods. In this work, we are specifically concerned with tomographic methods based on projection-backprojection reconstruction, a category that also includes the absorption tomography employed in radiology. When performed with a rotation about a single axis, the measurement of projections is mathematically described by the two-dimensional Radon transform, which may be written[19]

$$\mathcal{R}\big[f(x,y)\big](H,\phi) = \int_{-\infty}^{\infty} f\big(H(\sin\phi,\cos\phi) + s(\cos\phi,\sin\phi)\big)ds,$$

where $f(x,y)$ is some function on the plane, H is the scalar displacement (i.e., the signed orthogonal distance) of the line of projection from the axis of rotation, and ϕ is the angle of rotation. Thus, the Radon transform maps the two Cartesian coordinates of the function $f(x,y)$ in real space to one linear coordinate H and one angular coordinate ϕ in projected space. The inverse of this integral transform yields the Radon inversion formula, the mathematical

basis of the common reconstruction method of filtered backprojection. Although any function that can be expressed in a linear basis of scalars, such as a tensor field, could in principle be reconstructed simply by inverting the Radon transform for each scalar, it is not in general possible to completely determine the projections of such functions from individual measurements. This is the case for SAXS tensor tomography, where for each volume element, only a single cut of the three-dimensional reciprocal space map is measured with each projection. To increase the amount of information available for reconstruction, it is necessary to introduce an additional degree of freedom in the form of an axis of tilt. This means that it is no longer possible to reduce the problem to two dimensions, and a more general integral transform needs to be used. A suitable choice for this is the John transform, also known as the x-ray transform, which is one possible generalization of the Radon transform to three dimensions [19]. It may be written

$$\mathbb{X}[f(\mathbf{r})](j,k,\alpha,\beta) = \int_{-\infty}^{\infty} f\big(\mathbf{v}(j,k,\alpha,\beta) + s\mathbf{u}(\alpha,\beta)\big)ds, \tag{2.8}$$

where α is an angle in the xz-plane, β is the angle of elevation with respect to this plane, and the j and k may be regarded as the Cartesian coordinates of each projection plane. The full set of projection planes is described by defining the vector-valued functions $\mathbf{v}$ and $\mathbf{u}$ as

$$\mathbf{v} = j(\cos\alpha, 0, -\sin\alpha) + k(\sin\alpha\sin\beta, \cos\beta, -\cos\alpha\sin\beta), \tag{2.9}$$

which for fixed α and β describes a two-dimensional plane embedded in three-dimensional space, orthogonal to

$$\mathbf{u} = (\sin\alpha\cos\beta, \sin\beta, -\cos\alpha\cos\beta), \tag{2.10}$$

which describes the direction of projection in three dimensions. In Fig. 2.2 a schematic illustration of the coordinates in the John transform, (j,k,α,β), is shown relative to the sample coordinate system. The red line is the line of integration, mapped by the displacement vector $\mathbf{v}$ and the projection direction vector $\mathbf{u}$. These definitions are not unique, but instead correspond to a particular experimental arrangement in a laboratory frame where the positive z-direction is given by the direction in which the x-ray beam impinging on the sample travels, the y-axis is defined to be opposed to the direction of the

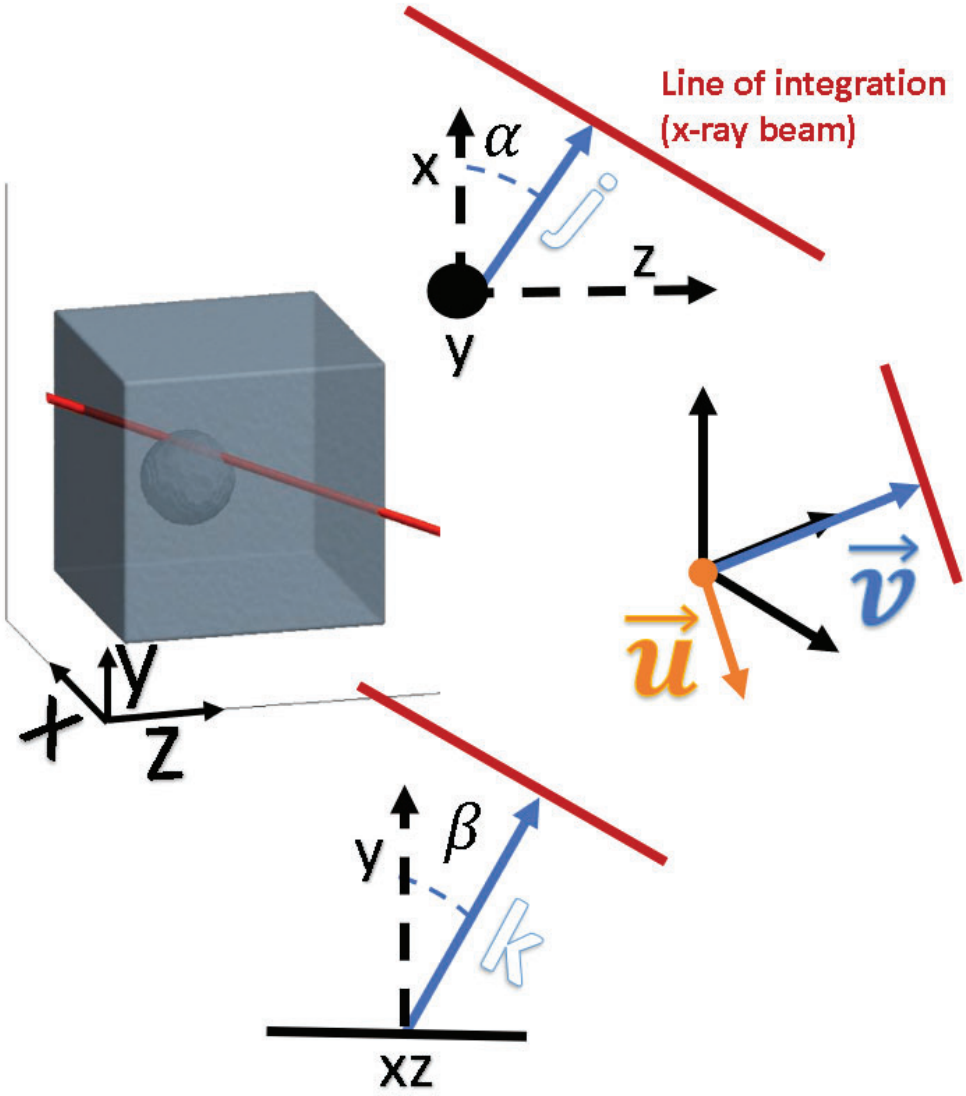

Figure 2.2: Schematic illustration of the coordinates in the John transform (Eq. (2.8)) in the sample coordinate system. The red line illustrates the line of integration, that is, the x-ray beam. (j, k) correspond to (x, y) in the laboratory frame, and to the two linear coordinates of the projection. **u** (labelled $\vec{u}$ in the figure for clarity) is the direction of integration (Eq. (2.10)), and **v** (labelled $\vec{v}$ in the figure for clarity) is the displacement of the line of integration from the origin.

local gravitational field, and the x-axis is defined by the right-hand rule.

The sample is first rotated about the y-axis by $-\alpha$, and then rotated about the x-axis by $-\beta$. Equations (2.8), (2.9), and (2.10) then describe the projections collected in terms of a sample coordinate system which is aligned with the laboratory frame when $\alpha = \beta = 0$

Inserting our model for the reciprocal-space-map tensor field from Eq. (2.2) into the John transform in Eq. (2.8), we obtain

$$\begin{aligned}&\mathbb{X}[M](\theta, \phi, j, k, \alpha, \beta) \\ &\quad = \sum_{\ell=0,2}^{\ell_{\max}} \sum_{m=-\ell}^{\ell} \hat{Y}_m^\ell(\theta, \phi) \int_{-\infty}^{\infty} a_m^\ell\big(\mathbf{v}(j, k, \alpha, \beta) + s\,\mathbf{u}(\alpha, \beta)\big) ds, \end{aligned} \tag{2.11}$$

This integral can be evaluated separately for each coefficient $a_m^\ell(\mathbf{r})$, and we may therefore write

$$\mathbb{X}[M](\theta, \phi, j, k, \alpha, \beta) = \sum_{\ell=0,2}^{\ell_{\max}} \sum_{m=-\ell}^{\ell} \hat{Y}_m^\ell(\theta, \phi)\, A_m^\ell(j, k, \alpha, \beta), \tag{2.12}$$

where $A_m^\ell(j, k, \alpha, \beta)$ is the spherical harmonic coefficient in projected space that corresponds to the integral of $a_m^\ell(\mathbf{r})$ over the corresponding to (j, k, α, β) in real space. For brevity, we introduce a shorthand notation for these coordinates,

$$\overline{\upsilon} \equiv (\upsilon_1, \upsilon_2, \upsilon_3, \upsilon_4) \equiv (j, k, \alpha, \beta),$$

such that $\overline{\upsilon}$ represents both a line of integration in real space, a point in projected space, and the experimental parameters that define the position and direction of the x-ray beam relative to the sample. A SAXS measurement spans only a great circle on the projected harmonic described by Eq. (2.12). Since this great circle is orthogonal to the direction of projection, we may use Eq. (2.9) to parameterize it as

$$C(t, \alpha, \beta) = \mathbf{v}(\cos(t), \sin(t), \upsilon_3, \upsilon_4). \tag{2.13}$$

We are now able to write a complete model for a SAXSTT dataset as

$$\mathcal{I}_M(t,\overline{\upsilon}) = \sum_{\ell=0,2}^{\ell_{\max}} \sum_{m=-\ell}^{\ell} \hat{Y}_m^\ell\big(C(t,\upsilon_3,\upsilon_4)\big)\, A_m^\ell(\overline{\upsilon}), \tag{2.14}$$

where $\mathcal{I}_M(t,\overline{\upsilon})$ models the transmission-normalized measured intensity $I_N(t,\overline{\upsilon})$. The five independent parameters in Eq. (2.14), (t,j,k,α,β) map directly to five parameters in the laboratory frame. Respectively, t maps to the azimuthal angle on the detector, (j,k) map to the (x,y) position of the sample relative to the x-ray source, and (α,β) map to the rotation and tilt of the sample.

2.4 Optimization and reconstruction

The reconstruction of the tensor field, which encodes the reciprocal space maps and geometry of a measured sample, is the inverse problem of determining $M(\mathbf{r},\theta,\phi)$ (Eq. (2.2)), given a set of measurements $I_N(t,\overline{\upsilon})$. This is done by means of the model in Eq. (2.14). This equation describes, however, a surjective relationship — it is not possible to determine every A_m^ℓ given a set of measurements $I_N(t,\overline{\upsilon})$ for a fixed $\overline{\upsilon}$. The degeneracy of the system is easiest to see in a coordinate system where $\theta = 0$, or in other words, choosing an $\overline{\upsilon}$ such that

$$\hat{Y}_m^\ell\big(C(t,\upsilon_3,\upsilon_4)\big) = \hat{Y}_m^\ell\big(0,t\big). \tag{2.15}$$

Any spherical harmonic can be represented in the same basis irrespective of any rotation of the coordinate system, so there is no loss of generality in this choice. We are able to interpolate any one set of n measurements using a trigonometric polynomial:

$$I_N(t,\overline{\upsilon}) = \sum_{m=0,2}^{\ell_{\max}} \big[C_m\cos(mt) + C_{-m}\sin(mt)\big], \tag{2.16}$$

with $\ell_{\max}$ as in Eq. (2.1), and where each C_m is a real constant. But from the definition of the spherical harmonics, we see that this is satisfied for each m

by any harmonic that fulfills

$$\sum_{\ell=|m|}^{\ell_{\max}} A_m^\ell P_{|m|}^\ell(0) = C_m, \tag{2.17}$$

where $P_{|m|}^\ell(0)$ is the associated Legendre polynomial of degree m and order ℓ. The solution to Eq. (2.17) is unique when and only when $|m| = \ell_{\max}$. For this reason, the non-scalar case (i.e., when $\ell_{\max} > 0$) is ill-posed and cannot be solved by direct means, such as by employing the Radon inversion formula. Instead, all measurements must be considered and an optimization problem must be solved. It is most straightforward to do this using a discrete formalism. We define for each measurement the squared residual,

$$\mathcal{R}_{i,j} = \left(\mathcal{I}_M(t_j, \overline{v}_i) - I(t_j, \overline{v_i})\right)^2, \tag{2.18}$$

which is then summed over all measurements and combined with a regularization function to yield the objective function,

$$\mathcal{O} = \sum_i \sum_j \left[w(t_j, \overline{v}_i)\, \mathcal{R}_{i,j}\right] + \Lambda(M), \tag{2.19}$$

where $w(t, \overline{v})$ is a weight function that reduces the influence of or nullifies low-quality or absent measurements, and Λ_i is a regularization function. The first term in Eq. (2.19) represents a weighted least squares fit of the model parameters to the data. However, given that the problem of tensor tomographic reconstruction is both large and ill-posed, it is not suitable to attempt to find a solution by only minimizing this term. The regularizing function Λ imposes additional constraints on the solution, consisting of the (discrete) tensor field M, and the choice of Λ is important for the performance and result of the optimization.

First, the reciprocal space maps encoded in M model scattering intensities measured using single-photon counting statistics. For this reason, we can impose the assumption that the uncertainty associated with each scattering element is proportional to its intensity by using the "hybrid" norm [20],

$$\Lambda_1(M) = \sum_i \sum_\ell \lambda_1(\ell) \sqrt{S_\ell(M_i, M_i)}, \tag{2.20}$$

where $\lambda_1(\ell)$ denotes a regularization coefficient function that may be a constant, or different for each ℓ. This is preferred over the standard L_1 norm, the sum of absolute coefficients, as that norm is not a rotational invariant. This will discourage the solution from including elements which do not sufficiently reduce the residuals in proportion to their absolute magnitude.

Secondly, it is common for measurements to include spurious data points which are large in intensity but which do not follow basic assumptions of the method, in particular from edge scattering. To reduce the effect of such outliers, one can include an L_2 regularization term, such as

$$\Lambda_2(M) = \sum_i \sum_\ell \lambda_2(\ell) S_\ell(M_i, M_i), \tag{2.21}$$

where $\lambda_2(\ell)$ is a function of the extent to which each order ℓ of the reciprocal space map contributes to the regularization. For example, one might wish to only regularize large anisotropic intensities, in which case one would set $\lambda_\ell(0) = 0$.

Finally, one can impose an expectation of continuity and correlation length by including a factor based on the similarity of each order of neighbouring reciprocal space maps, for example,

$$\Lambda_\rho(M) = \sum_i \sum_j \sum_\ell \rho_{i,j}(\ell)\big(S_\ell(M_i, M_i) + S_\ell(M_j, M_j) - 2S_\ell(M_i, M_j)\big), \tag{2.22}$$

where $\rho_{i,j}(\ell)$ is a function that encodes the weight of the regularization factor and the expected correlation length, and S_ℓ is the inner product relating to the norm, variance and covariance of the reciprocal space map as per equations (2.4) (2.5), and (2.6). In practice, Eq. (2.22) can be computationally overwhelming for large optimizations, but it can be used, for example, to impose an expectation of correlation between neighbors with relative ease.

The values of the associated hyperparameters, λ_1, λ_2, and $\rho_{i,j}$, typically need to be determined by a systematic search over several orders of magnitude, which can consume a non-negligible amount of computational time, as each trial requires at least a partial reconstruction to be performed.

Regardless of the choice of regularization, which will depend on the data set one from which one wishes to compute a reconstruction, it is necessary to minimize Eq. (2.19) with respect to the tensor field M. The size of the

reconstruction (generally ranging from millions to tens of millions of coefficients) makes it necessary to use a gradient-based solver, which necessitates the computation of the gradient of the objective function (2.19), including the regularization terms, with respect to every element of the tensor field M. Implicitly, computing the derivative of the objective function also entails computing the back-projection, which is effectively the geometric inversion of the projection integral in Eq. (2.12). There are several possible choices for gradient-based solvers, such as the conjugate gradient method; the approach used in this work is the limited-memory BFGS algorithm, as implemented in the SciPy package `scipy.optimize` [21]. The code used for reconstruction in this work consists of a wrapper written in Python, code for computing the objective function and its gradient written in C, as well as utility functions for computing spherical harmonics written in Fortran. Three-dimensional visualizations were created using Mayavi [22]. This implementation is referred to as Real Unrestricted Spherical Harmonic Tensor Tomography (RUSHTT).

2.5 Simulations

Due to the ill-posed nature of the problem of tensor tomography, it is useful to be able to explore any reconstruction method in a simulated environment. This helps examine the reliability of the method and the conditions required for producing an adequate reconstruction, such as the maximum tilt angle and number of projections that need to be used. The most straightforward way to develop a simulation model is to base it on the formalism described in this chapter. To do so, artificial three-dimensional tensor fields M consisting of a distribution of spherical harmonics are created, represented by spherical harmonics. The basic intensity of each volume element is specified in terms of the mean, or isotropic intensity (given by the coefficient of $\hat{Y}_0^0$). Each volume element is assigned a symmetry represented by a linear combination of $\ell > 0$ spherical harmonics, which is then given a magnitude specified by a relative coefficient that represents the strength of the anisotropy. The field is then projected at angles which lie on a Kurihara mesh, which is a useful distribution for representing measurements evenly distributed on the sphere which lie at fixed angles of elevation, and a number of points on each great circle of small-angle scattering (Eq. (2.13)) are recorded [23]. To these data points, Poisson noise is added, which has a variance directly proportional to the intensity.

This differs somewhat from real measurements which also involve correction by a transmission factor, and therefore their noise is not fully correlated to the normalized scattering intensity. Omitting this factor in the simulated data removes, however, the necessity of modeling the transmittivity of the sample, while maintaining a reasonable noise model. The result is a data set that can be fed into a SAXSTT reconstruction algorithm, and the output of the algorithm can be compared to the original. For more details on the simulation formalism, see Paper I.

CHAPTER 3

Results and discussion

3.1 Regularization and reconstruction

To determine the appropriate regularization coefficients for a reconstruction, the L-curve method is used. This entails doing multiple trial reconstructions with different coefficients and comparing the change in the regularization term to the change in the function residuals, to choose a coefficient which reduces the regularization norm by a large amount, while having a relatively small effect on the residual norm.

Figure 3.1 shows the selection of the three regularization coefficients by means of L-curve tests (see Eqs. (2.20), (2.21), and (2.22) for the expressions). The coefficients are chosen and set successively: first, the coefficient for the hybrid norm is determined (using all ℓ), then for the correlation-length norm (using only $\ell > 0$), and finally the L_2 norm (again, using only $\ell > 0$). The reason for using only $\ell > 0$ for the covariance and L_2 regularization terms is that the primary reasons for these regularization terms are to impose an expectation of continuity in the symmetries of the anisotropic part of the reciprocal space map, and to suppress effects like edge scattering. On the other hand, the purpose of the hybrid regularization is to encode the relationship

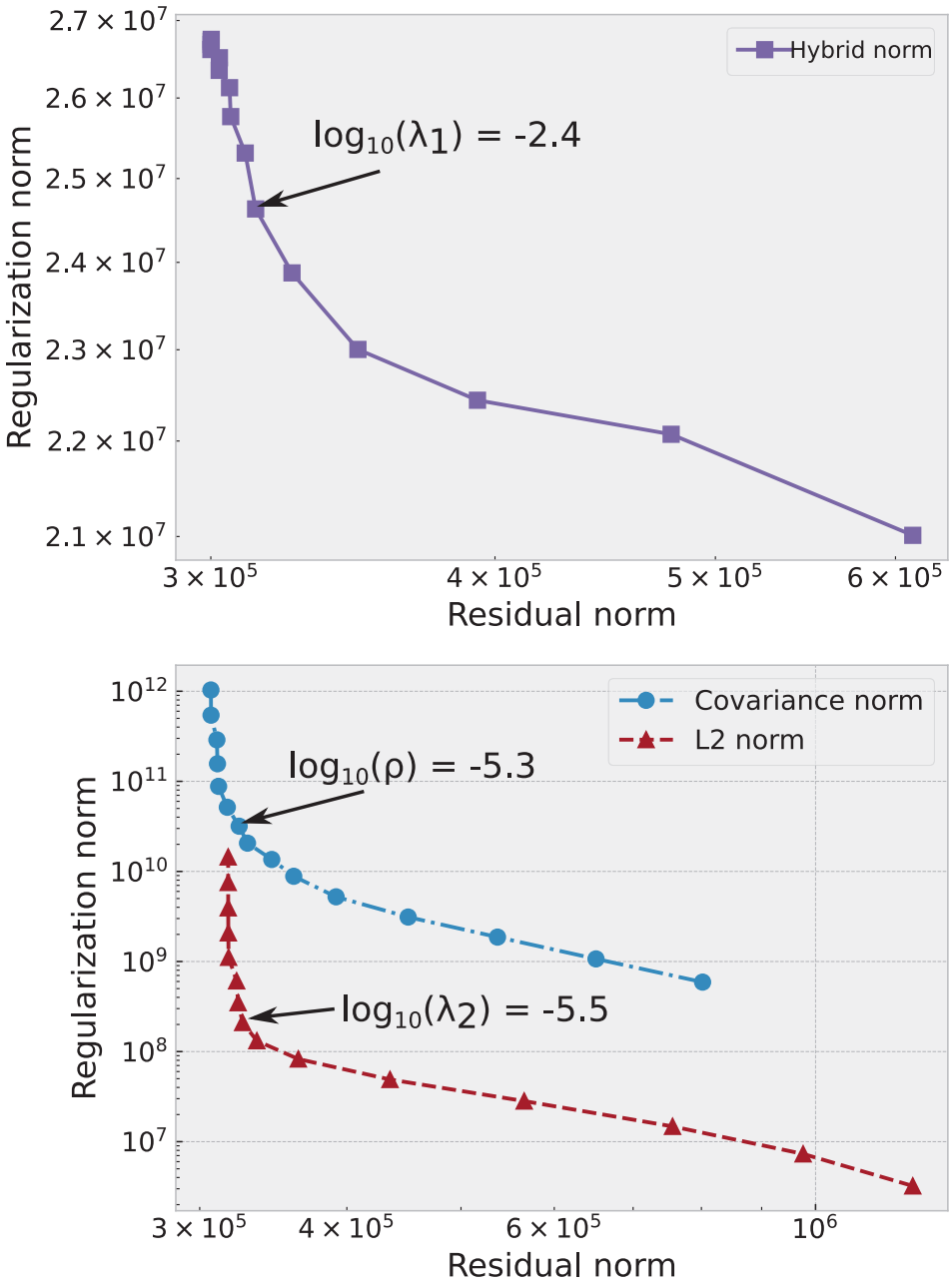

Figure 3.1: L-curve tests for the three different regularization norms used in RUSHTT (see Eqs. (2.20), (2.21), and (2.22)). The coefficients (λ_1, ρ, and λ_2) are given values ranging over several orders of magnitude to find a suitable value, that reduces the regularization norm without affecting the residual norm too much.

between uncertainty and intensity in the data, which requires the use of all orders.

Figure 3.2 shows the effect of covariance regularization on figure orientations. (a) is unregularized, whereas (b) has a regularization factor of 10^{-5}, (c) has a factor of 10^{-4}, and (d) has the factor 10^{-3}. As is also suggested by Figure 3.1, a value around 10^{-5} is a good choice for this regularization, increasing continuity without eliminating features, whereas higher values lead to overregularization.

Using the regularization parameters determined in Figure 3.1, the reconstruction in Figure 3.3 was obtained.

3.2 Comparison to previous SAXSTT models

To investigate the performance of RUSHTT, it has been compared to two previous methods for SAXS tensor tomography which use similar input data and comparable approaches to reconstruction. The first is the Spherical Harmonic (SH) method presented by Liebi *et al.* (2015, 2018) [15][16], on which RUSHTT is based. While Liebi *et al.* (2018) [16] describes the possibility of using a complete basis of spherical harmonics up to a maximum order, the present implementation of SH uses only the $m = 0$ harmonics, along with two Euler angles, which specify fiber- or point-symmetric orientations in the sample. Moreover, SH employs squared even-ordered spherical harmonics in each volume element, which means that it is fitting measured data to a sum of squared basis functions and coefficients. The approach uses a conjugate gradient algorithm to perform the reconstruction. The second method is the Iterative Reconstruction (IR) approach of Gao *et al.* (2018) [24]. This approach represents the reciprocal space map in using a symmetric rank-2 tensor field in matrix representation, which is isomorphic to a field of even-ordered real spherical harmonics of $\ell = 0, 2$. Rather than determine the intensity projected from the great circle on the reciprocal space map, comparing this to the measurement, and then computing the gradient, the method pretransforms the measured intensities into tensor components. It then directly obtains the gradient as the difference between the action of the projected tensor field on the points of measurement and the transformed intensities. The difference is then minimized by back-projecting the gradient and using the method of steepest gradient descent with constant step size. These methods have been compared

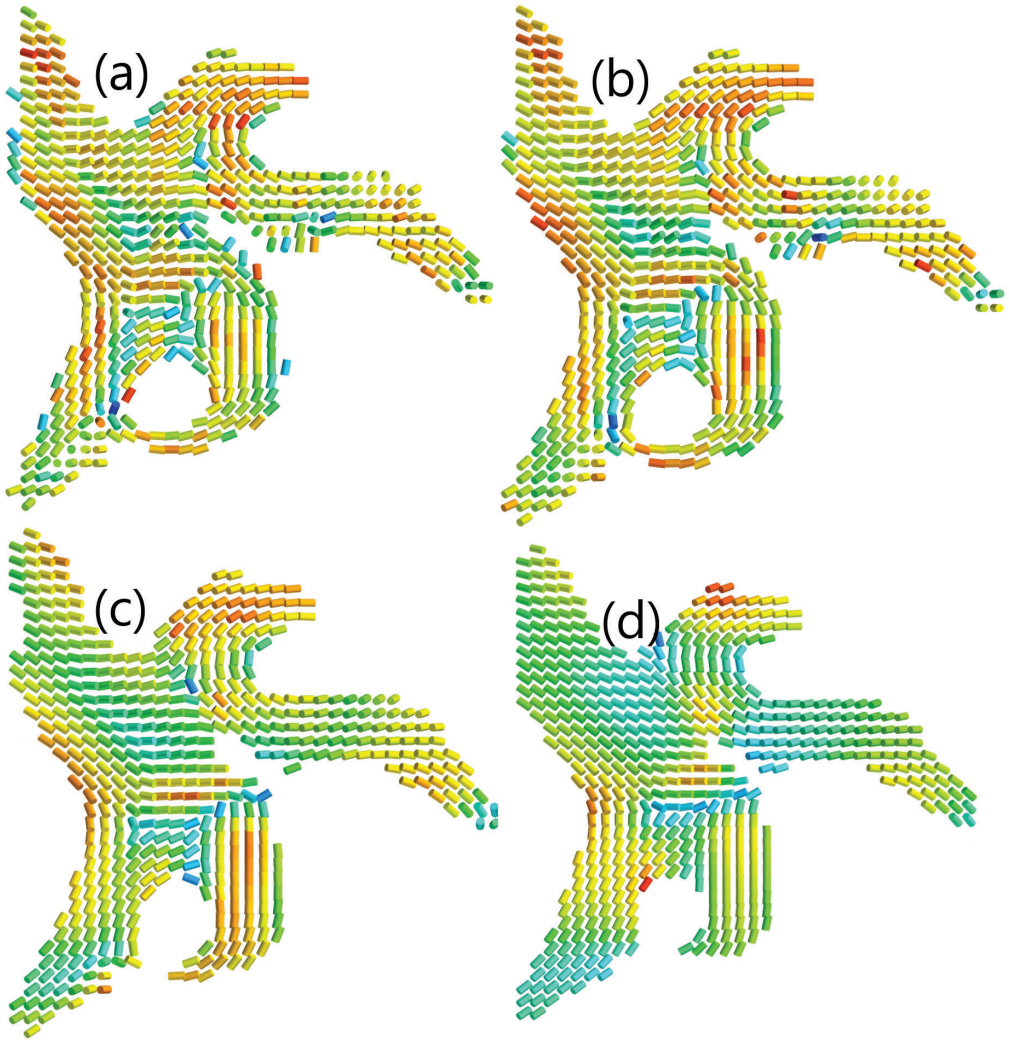

Figure 3.2: Comparison of trabecular bone sample between different levels of covariance regularization (Eq. (2.22)). For experimental details, see Liebi *et al.* (2018, sample B) [16]. (a) shows the result with no regularization, (b) shows the result with the regularization coefficient 10^{-5}, (c) with 10^{-4}, and (d) with 10^{-3}. The color indicates the relative magnitude of the eigenvalue associated with the orientation eigenvector of the Rank 2-tensor. While (a) is already relatively continuous, the eigenvalue distribution appears somewhat discontinuous, and some orientations seem to go against the trend. (b) is more regular and suggests that a value around 10^{-5} could be a good choice for the regularization, whereas (c) and (d) look excessively smooth to the point of eliminating features, suggesting their regularization coefficient is too large.

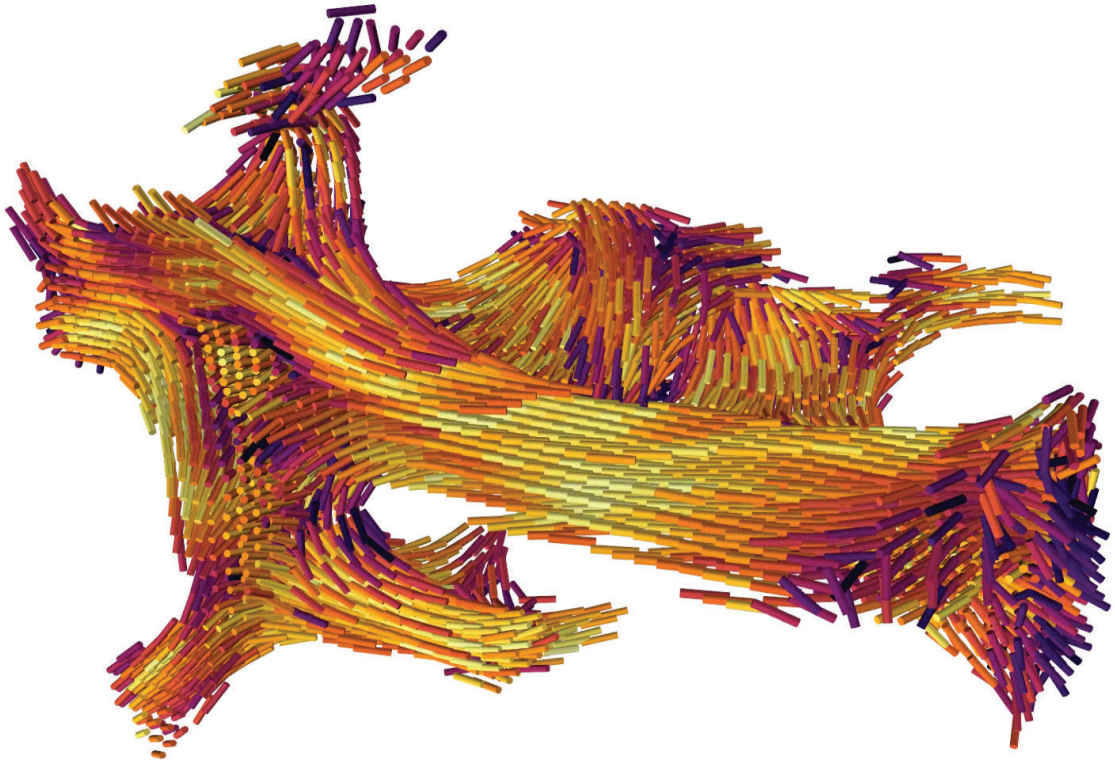

Figure 3.3: Reconstruction of trabecular bone sample. For experimental details, see Liebi *et al.* (2018, sample B) [16]. A cut has been made along the middle to expose the interior of the reconstruction. The coloring corresponds to the symmetry of the rank-2 tensor; brighter means more fiber-like with a great circle band of scattering, darker means more point-like, with a polar "cap" of scattering.

in two cases - one using simulated data, and the other using measured data.

Simulation comparison

A simulated sample was created using only spherical harmonic basis functions up to $\ell = 2$. To make the sample as simple as possible in terms of tensor field symmetry, only the basis function $\hat{Y}_0^2$, combined with rotations, were used. The coefficient of the $\hat{Y}_0^0$ component of the tensors making up the sample itself (rather than empty space) was set to 5000, and the relative coefficient of the anisotropic part was set to $-1/7$. This simulated sample was then projected at angles evenly distributed on the sphere on a Kurihara mesh, up to a tilt of 45°, at varying numbers of noise and with varying numbers of data points. The difference between the orientation of the sample and the orientation retrieved by each of the methods was then determined to evaluate their performance, per the equation

$$\delta(\mathbf{v_1}, \mathbf{v_2}) = \arccos \left| \frac{\mathbf{v_1} \cdot \mathbf{v_2}}{\|\mathbf{v_1}\| \, \|\mathbf{v_2}\|} \right|. \tag{3.1}$$

The result of the comparison is seen in Fig. 3.4. In all cases, RUSHTT (in this case, with all regularization norms set to 0) is the best performing method both in terms of median error and interquartile range. IR outperforms SH in all cases except when 32 detector points are used, where SH has a slightly better median error but a larger interquartile range. The overall poorer performance of SH is at least in part explained by the fact that the method, unlike IR and RUSHTT, uses squared spherical harmonics, and thus cannot easily replicate the precise symmetry of the simulated sample's anisotropy. These results suggest that even in cases where the samples have a simple symmetry, RUSHTT gives more accurate reconstructions (Paper I).

Experimental comparisons

The three methods - SH, IR and RUSHTT were compared for performance and results using a sample of trabecular bone embedded in PMMA; for experimental details, see Liebi *et al.* (2018, sample B) [16]. In addition, a modified version of SH was created which does not use squared harmonics (here called SH (non-squared)), in order to better understand the differences between the results produced by the different methods. The tests were performed on a

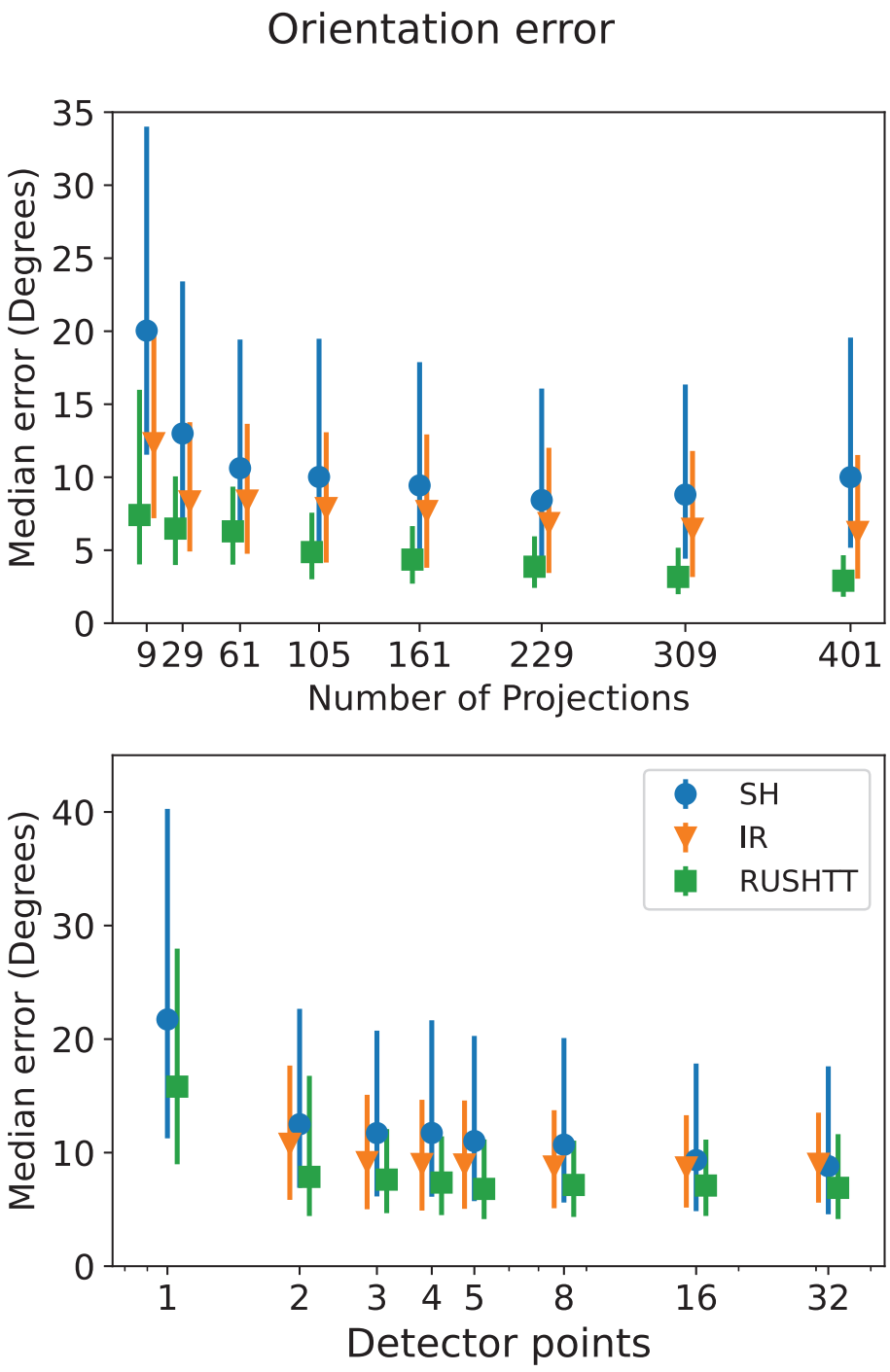

Figure 3.4: Comparing the orientation deviation between methods for reconstructing the simulated sample as functions of detector points and number of projections. The error is the median of the quantity defined in Eq. (3.1), excluding those voxels which are of zero intensity in the simulated sample. The error bars extend one interquartile range in each direction.

workstation using a 12-core, 4.6 GHz AMD Ryzen 9 3900X CPU, and 64 GB DDR4 2666 MHz RAM. Two tests were performed with RUSHTT - one using coefficients up to $\ell = 6$, the maximum order that can be fit to the 8 detector segments of the data, to compare its performance with SH. The other test used coefficients up to only $\ell = 2$; this basis is isomorphic to the symmetric rank-2 tensor used by IR, and therefore makes for an ideal comparison. All methods were subjected to simple optimizations, such as removing unnecessary outputs and plots during the reconstruction. Moreover, IR was modified to repeatedly iterate over all projections, rather than picking projections at random, in order to yield a smooth convergence curve; no difference in the final result was observed. This was necessary in order to give all the methods a similar termination condition; the chosen condition was for the relative improvement in the objective function for one iteration to fall below 10^{-3}; in the case of the SH methods, this condition was used for each step. The gradient often remains relatively large for real SAXSTT data, in part due to the presence of hard-to-fit features, including both edge-scattering as well as features in the sample reciprocal space map which are not completely resolved in all projections due to data reduction. For this reason, the size of the gradient was not considered in the termination condition. The SH method performs reconstructions in a step-wise manner and requires the specification of certain parameters. Initial guesses for the relative coefficients of the anisotropic components of the reciprocal space map must be provided; these were specified based on a combination of heuristics and information from the RUSHTT reconstruction. Additionally, a coefficient for the regularization of the Euler angles in the reciprocal space map needs to be determined based on L-curve calculations; these were precomputed and are not included in the timing test. For RUSHTT, regularization based on the hybrid norm, L_2 norm as well as nearest-neighbour correlation was employed; see section 3.1 for more discussion on how these parameters were determined. It is important to note that while IR and RUSHTT use the same residual norm (Eq. (2.18)), the two SH methods use a different norm, viz.,

$$\mathcal{S}_{i,j}(\mathcal{I}_M, I) = \left(\sqrt{\mathcal{I}_M(t,\overline{v})} - \sqrt{I(t,\overline{v})}\right)^2,$$

the squared difference of square roots. The use of this residual is motivated by a reasoning similar to that for the hybrid regularization (Eq. (2.20)), that is

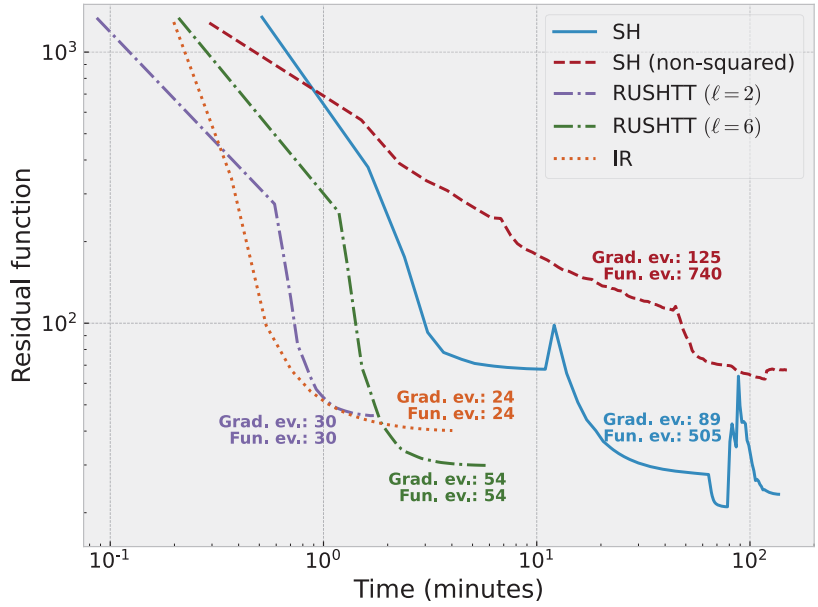

Figure 3.5: Comparison of residual function reduction over time for different methods. The text indicates the number of times each objective function and gradient function is evaluated. RUSHTT and IR both use the sum of squared differences as their residual function, whereas SH and SH (non-squared) use the sum of squared square-root differences.

the presence of noise which follows a Poisson distribution, with a variance proportional to the measured intensity. However, its usage in an objective function for gradient-based methods is associated with certain limitations, such as slow convergence when measurements vary over multiple orders of magnitude, which is why the squared difference combined with regularization is preferred for RUSHTT. The results of the performance tests with the residual of each function as a function of time to convergence are shown in Fig. 3.5. In the figures for SH and SH (non-squared), the step-wise nature of the optimization is apparent. The two methods converge in a different manner, which is to be expected, given that the usage of a square in the model of SH results in a different gradient of the residual. The time required for convergence of all steps is of the same order of magnitude, landing at 118 minutes for SH, and 149 minutes for SH (non-squared). SH achieves a greater reduction of its residuals

than its non-squared variants, but the two approaches should not be directly compared with respect to this quantity since they impose different symmetries on the reciprocal space map. RUSHTT is shown with two different settings, one with $\ell_{\max} = 2$ (6 coefficients) and one with $\ell_{\max} = 6$ (28 coefficients); they converge in 1.8 minutes and 5.8 minutes, respectively. With the setting $\ell = 6$ it achieves a greater reduction in its residuals than with $\ell = 2$, which is to be expected given that it has many more degrees of freedom which the data resolution is high enough to support. Finally, IR is seen to converge in 3.9 minutes, faster than RUSHTT with $\ell = 6$ but slower than RUSHTT with $\ell = 2$. While its residual function is in principle directly comparable to that of RUSHTT and shows a slightly lower final residual norm, IR is unregularized and permits negative values in the reconstruction to cancel out positive values. Negative values in the reconstruction reduce the constraints on its parameters in minimizing its residuals, but are not physically possible, and it is not straightforward to modify IR to eliminate this behaviour. For these two reasons, it is not surprising that IR achieves a slightly further reduction of its residuals. In general, the different methods use different basis functions, as well as different assumptions and constraints; consequently, the comparison's primary purpose is to compare their convergence behaviour, rather than the quality of their reconstructions. Fig. 3.6 shows an axial section of the reconstruction, with the output from four of the reconstructions compared in in Fig. 3.5 (with RUSHTT with $\ell = 2$ excluded). The bars show the principal orientation of each RSM, and are colored by the relative anisotropy, defined as the standard deviation divided by the mean, which is computed directly by sampling each reciprocal space map. The SH and the SH (non-squared) reconstructions are markedly different - despite regularization, the orientations in the SH section are not strongly correlated to their neighbours, in contrast to the SH (non-squared) reconstruction. SH (non-squared) has a very evenly distributed relative anisotropy, with little variation, whereas SH has a clearly defined texture with less anisotropy near the center and more near the edges. The distribution of anisotropy in RUSHTT is more similar to that in the SH section, while its orientations are more similar to those of SH (non-squared). The virtual slice from the IR reconstruction overall shows the lowest amount of anisotropy, but shows a smooth distribution of orientations broadly similar to those of SH (non-squared) and RUSHTT. Compared to SH (non-squared) and RUSHTT, its orientation distribution is somewhat "blocky", containing

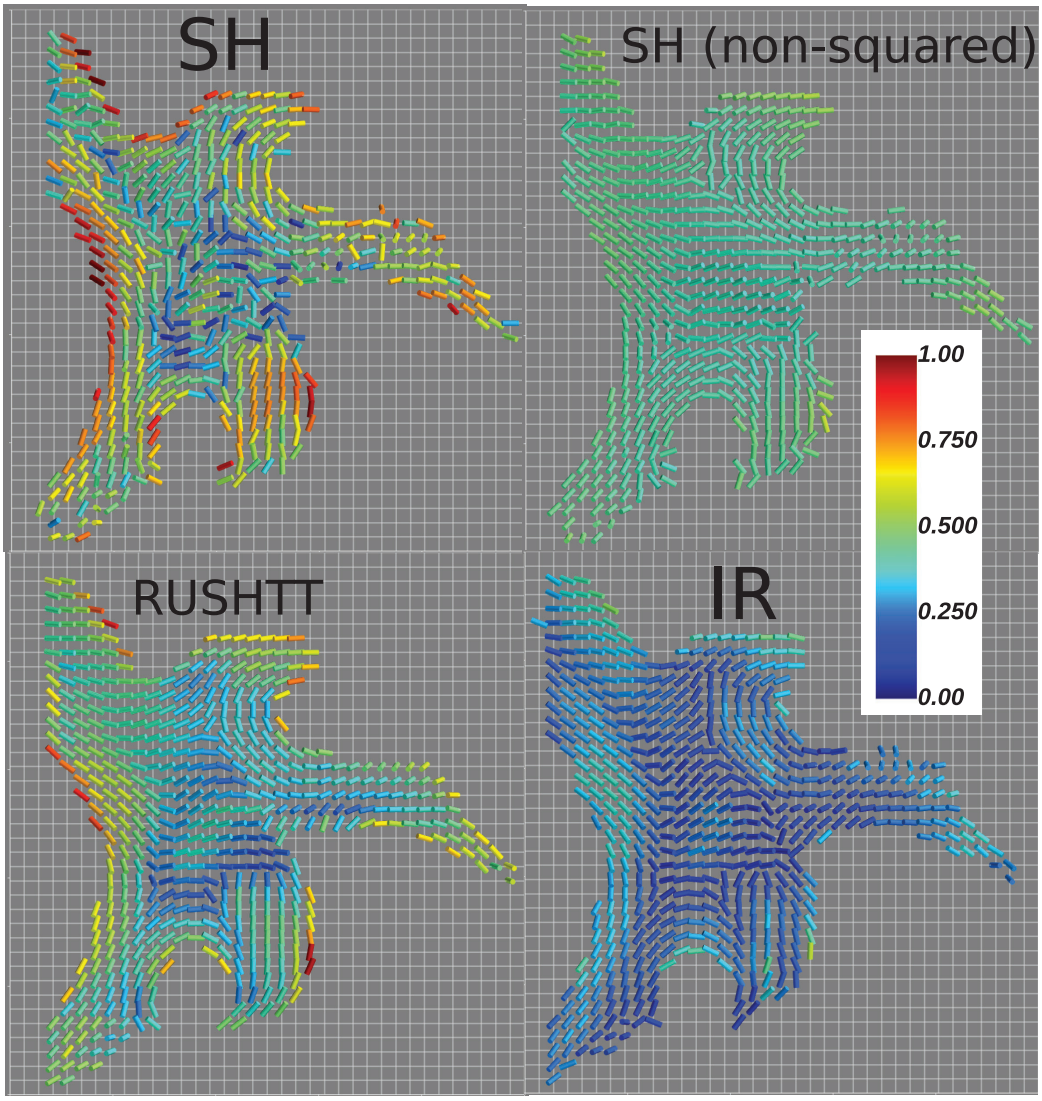

Figure 3.6: Virtual sections of four tensor tomographic reconstructions of the same dataset from a measurement of trabecular bone, using four different methods, colored by the amount of anisotropy in each reconstructed reciprocal space map, defined as the standard deviation of the intensity, divided by the mean. For experimental details, see Liebi *et al.* (2018, sample B) [16]. The orientations of the SH method are much less correlated to their neighbours than those of the other methods, including the SH (non-squared) method, which uses the same coefficients for its reciprocal space map model but does not square them. However, SH (non-squared) shows very little variation in its amount of anisotropy, compared to SH. RUSHTT (with $\ell_{\max} = 6$) shows a combination of smoothly varying orientations and a variation in the amount of anisotropy, similar to that of the SH method. The orientations in IR have the appearance of being divided into relatively uniform domains with sharper transitions between them; its amount of anisotropy is quite low, but displays some variation.

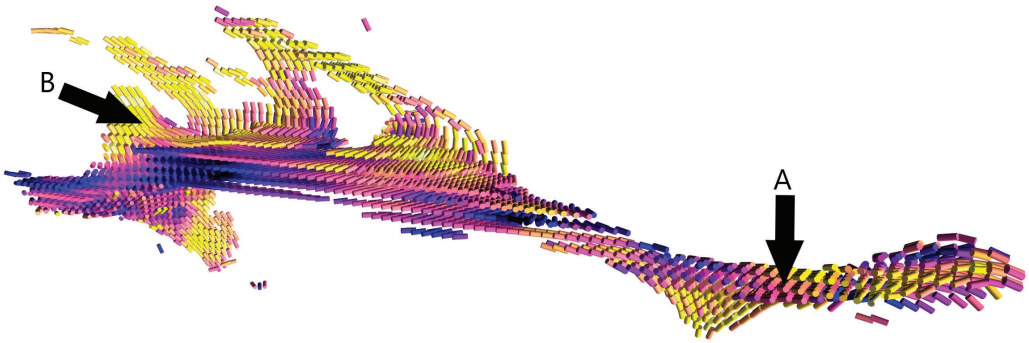

Figure 3.7: Volume render with eigenvector orientation bars of a reconstructed sample of trabecular bone. For experimental details, see Liebi *et al.* (2015) [15]. The arrows labeled A and B show the regions from which two subsets of reciprocal space maps have been extracted. A cut has been made along the long axis in the plane facing the reader to expose the sample interior.

several domains of largely uniform orientations, rather than continuous variation, compared to e.g. the upper left part of RUSHTT. This may be in part due to the limited symmetries available to the rank-2 tensor used by IR, as well as due to the algorithms used of fixed step size descent that is not adjusted based on rate convergence or approximations of higher derivatives. Such an interpretation would be consistent with IR's poorer performance compared to RUSHTT in the test with simulated data, shown in Fig. 3.4.

3.3 Multiple orientations

The Funk transform was applied to reciprocal space maps obtained from the reconstruction of a second trabecular bone sample. A volume render with orientation bars can be seen in Fig. 3.7. For experimental details, see Liebi *et al.* (2015) [15]. From the two areas A (an interior region) and B (an exterior, interface region) two subsets of reciprocal space maps have been extracted. In Fig. 3.8, the relationship between the Funk transformed reciprocal space maps obtained from regions A and B and the orientations extracted from them are shown. The interior region A is uniformly oriented, whereas the interface region B where several orientations come together, has two orientations.

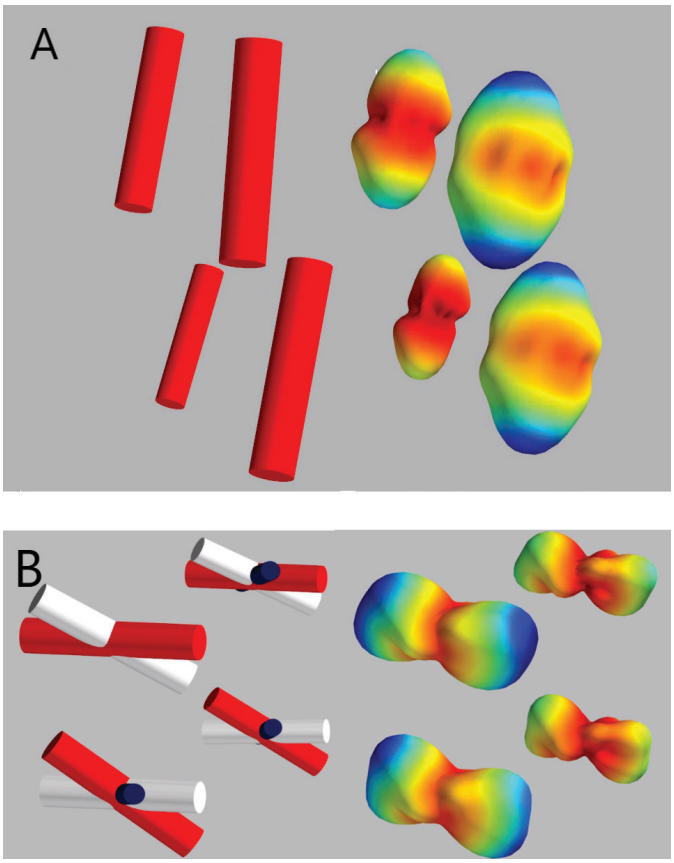

Figure 3.8: Multi-orientation analysis of Funk transformed reciprocal space maps from trabecular bone reconstruction, extracted by identifying local maxima. The single orientation of A, from an interior region, can be contrasted to the multi-orientation of B, which comes from an exterior interface region. The radius of the transformed reciprocal space map shows the Funk transform, whereas the coloring show sthe symmetry of the untransformed reciprocal space map.

CHAPTER 4

Concluding Remarks and Future Work

RUSHTT is able to reconstruct reciprocal space maps in a manner that is faster and more general than previous methods. Moreover, it is easy to regularize through the incorporation of pre-existing knowledge of the sample, owing to the straightforwardness of expressing quantities such as variance and covariance in terms of spherical harmonic inner products. It has been shown using simulations that even in relatively simple cases such as retrieving the orientations of reciprocal space maps with rank-2 tensor symmetry, the approach of SAXSTT performs better than the methods of Liebi *et al.* (2018) [16] and Gao *et al.* (2019) [24]. It has also been demonstrated that it is possible to retrieve sub-voxel information such as overlapping orientation through analysis of the reciprocal space maps.

For future work, the decrease in required computational time, as well as the array of options for power spectrum-based regularization, would make it possible to perform q-resolved reconstructions in an efficient and reliable manner, where for example successive reconstructions of individual q-ranges can be regularized by demanding some amount of correlation to the previous q-range. The many symmetries available from the real spherical harmonics, meanwhile, opens the door to tomographic reconstruction of samples with

full three-dimensional reciprocal space maps of greater complexity than has previously been possible.

In addition, the development of a robust, versatile and computationally efficient method and implementation of SAXSTT is a crucial step on the way toward an accessible software package that can suit the needs of scientific facilities as well as external end-users. Implementing SAXSTT at a beamline and collecting datasets involves the choice of many experimental parameters, such as the coordinate system, rotation axes, relative detector orientation, scanning resolution, exposure time, and so on, which must be taken into account by the reconstruction. Additionally, processing the many terabytes of data typically collected involves extensive data reduction, and the way in which the data is reduced imposes assumptions on the reconstruction. A rigorous method anchored in integral geometry with a general, vector-based formalism would be highly useful for deriving the general transforms needed to perform SAXSTT reconstruction. Additionally, such a method makes explicit the limits imposed by data reduction on the reconstruction, which can inform the choices made in setting up SAXSTT infrastructure. Moreover, information specific to a particular measurement, such as data statistics, can be incorporated into the reconstruction via regularization.

Creating such a software package in a modular manner based on the established formalism, it would be possible to accommodate different users in different situations. Demanding components of the reconstruction, such as the computation of integral transforms, can be implemented both in parallelized CPU-based form with simplifying approximations, suitable for computation on ordinary workstations, as well as using very accurate high-speed GPU-based algorithms. The package can be extended with components for future development, such as reconstruction algorithms for wide angle x-rate scattering tensor tomography, or real-time reconstruction during data collection.

With respect to future development of real-time reconstruction, it will be highly useful to have the theoretical description of the relationship between measurement and reconstruction established in this work, on which the method of data collection and real-time reduction can be based, as well as versatile means of regularizing and correlating successive reconstructions. The possibility of performing a real-time reconstruction during measurement which can give direct feedback on when enough data has been collected will be vital in using synchrotron time in the most efficient way possible.

References

[1] P. Fratzl, S. Schreiber, and K. Klaushofer, "Bone mineralization as studied by small-angle x-ray scattering," *Connective Tissue Research*, vol. 34, no. 4, pp. 247–254, 1996.

[2] M. Georgiadis, R. Müller, and P. Schneider, "Techniques to assess bone ultrastructure organization: Orientation and arrangement of mineralized collagen fibrils," *Journal of The Royal Society Interface*, vol. 13, no. 119, p. 20 160 088, 2016.

[3] H. Lichtenegger, M. Müller, O. Paris, C. Riekel, and P. Fratzl, "Imaging of the helical arrangement of cellulose fibrils in wood by synchrotron X-ray microdiffraction," *Journal of Applied Crystallography*, vol. 32, no. 6, pp. 1127–1133, Dec. 1999.

[4] P. Fratzl, H. F. Jakob, S. Rinnerthaler, P. Roschger, and K. Klaushofer, "Position-Resolved Small-Angle X-ray Scattering of Complex Biological Materials," *Journal of Applied Crystallography*, vol. 30, no. 5 Part 2, pp. 765–769, Oct. 1997.

[5] S. Pabisch, W. Wagermaier, T. Zander, C. Li, and P. Fratzl, "Chapter eighteen - imaging the nanostructure of bone and dentin through small- and wide-angle x-ray scattering," in *Research Methods in Biomineralization Science*, ser. Methods in Enzymology, J. J. De Yoreo, Ed., vol. 532, Academic Press, 2013, pp. 391–413.

[6] O. Paris, "From diffraction to imaging: New avenues in studying hierarchical biological tissues with x-ray microbeams (review)," *Biointerphases*, vol. 3, no. 2, FB16–FB26, 2008.

[7] Y. Liu, I. Manjubala, P. Roschger, H. Schell, G. N. Duda, and P. Fratzl, "Mineral crystal alignment in mineralized fracture callus determined by 3d small-angle x-ray scattering," *Journal of Physics: Conference Series*, vol. 247, p. 012 031, Oct. 2010.

[8] R. Seidel, A. Gourrier, M. Kerschnitzki, *et al.*, "Synchrotron 3d saxs analysis of bone nanostructure," *Bioinspired, Biomimetic and Nanobiomaterials*, vol. 1, no. 2, pp. 123–131, 2012.

[9] J. M. Feldkamp, M. Kuhlmann, S. V. Roth, *et al.*, "Recent developments in tomographic small-angle x-ray scattering," *physica status solidi (a)*, vol. 206, no. 8, pp. 1723–1726, 2009.

[10] C. G. Schroer, M. Kuhlmann, S. V. Roth, *et al.*, "Mapping the local nanostructure inside a specimen by tomographic small-angle x-ray scattering," *Applied Physics Letters*, vol. 88, no. 16, p. 164 102, 2006.

[11] N. Stribeck, U. Nöchel, S. S. Funari, and T. Schubert, "Tensile tests of polypropylene monitored by saxs. comparing the stretch-hold technique to the dynamic technique," *Journal of Polymer Science Part B: Polymer Physics*, vol. 46, no. 7, pp. 721–726, 2008.

[12] M. Álvarez-Murga, P. Bleuet, and J.-L. Hodeau, "Diffraction/scattering computed tomography for three-dimensional characterization of multiphase crystalline and amorphous materials," *Journal of Applied Crystallography*, vol. 45, no. 6, pp. 1109–1124, Dec. 2012.

[13] T. H. Jensen, M. Bech, O. Bunk, *et al.*, "Molecular x-ray computed tomography of myelin in a rat brain," *NeuroImage*, vol. 57, no. 1, pp. 124–129, 2011, ISSN: 1053-8119.

[14] F. Schaff, M. Bech, P. Zaslansky, *et al.*, "Six-dimensional real and reciprocal space small-angle x-ray scattering tomography," *Nature*, vol. 527, no. 7578, pp. 353–356, Nov. 2015.

[15] M. Liebi, M. Georgiadis, A. Menzel, *et al.*, "Nanostructure surveys of macroscopic specimens by small-angle scattering tensor tomography," *Nature*, vol. 527, no. 7578, pp. 349–352, 2015.

[16] M. Liebi, M. Georgiadis, J. Kohlbrecher, *et al.*, "Small-angle X-ray scattering tensor tomography: model of the three-dimensional reciprocal-space map, reconstruction algorithm and angular sampling requirements," *Acta Crystallographica Section A*, vol. 74, no. 1, pp. 12–24, Jan. 2018.

[17] O. Glatter, O. Kratky, and H. Kratky, *Small angle X-ray scattering*. Academic press, 1982.

[18] M. A. Wieczorek and M. Meschede, "Shtools: Tools for working with spherical harmonics," *Geochemistry, Geophysics, Geosystems*, vol. 19, no. 8, pp. 2574–2592, 2018.

[19] R. Ramlau and O. Scherzer, *The Radon Transform: The First 100 Years and Beyond*, ser. Radon series on computational and applied mathematics. De Gruyter, 2019, ISBN: 9783110559415.

[20] Q. T. Le Gia, I. H. Sloan, R. S. Womersley, and Y. G. Wang, "Isotropic sparse regularization for spherical harmonic representations of random fields on the sphere," *Applied and Computational Harmonic Analysis*, vol. 49, no. 1, pp. 257–278, 2020, ISSN: 1063-5203.

[21] P. Virtanen, R. Gommers, T. E. Oliphant, *et al.*, "SciPy 1.0: Fundamental Algorithms for Scientific Computing in Python," *Nature Methods*, vol. 17, pp. 261–272, 2020.

[22] P. Ramachandran and G. Varoquaux, "Mayavi: 3D Visualization of Scientific Data," *Computing in Science & Engineering*, vol. 13, no. 2, pp. 40–51, 2011, ISSN: 1521-9615.

[23] Y. Kurihara, "Numerical integration of the primitive equations on a spherical grid," *Monthly Weather Review*, vol. 93, no. 7, pp. 399–415, 1965.

[24] Z. Gao, M. Guizar-Sicairos, V. Lutz-Bueno, *et al.*, "High-speed tensor tomography: iterative reconstruction tensor tomography (IRTT) algorithm," *Acta Crystallographica Section A*, vol. 75, no. 2, pp. 223–238, Mar. 2019.